Published in final edited form as:

Dev Biol. 2024 August ; 512: 44–56. doi:10.1016/j.ydbio.2024.05.005.

Forward genetics combined with unsupervised classifications identified zebrafish mutants affecting biliary system formation

Divya Jyoti Singh[a,1], **Kathryn M. Tuscano**[a,1], **Amrhen L. Ortega**[a], **Manali Dimri**[a], **Kevin Tae**[a], **William Lee**[a], **Muslim A. Muslim**[a], **Isabela M. Rivera Paz**[a], **Jay L. Liu**[a], **Lain X. Pierce**[a], **Allyson McClendon**[a], **Isabel Gibson**[a], **Jodi Livesay**[a], **Takuya F. Sakaguchi**[a,b,*]

[a]Department of Inflammation and Immunity, Lerner Research Institute of Cleveland Clinic, Cleveland, OH, 44195, USA

[b]Department of Molecular Medicine, Cleveland Clinic Lerner College of Medicine of Case Western Reserve University, Cleveland, OH, 44195, USA

Abstract

Impaired formation of the biliary network can lead to congenital cholestatic liver diseases; however, the genes responsible for proper biliary system formation and maintenance have not been fully identified. Combining computational network structure analysis algorithms with a zebrafish forward genetic screen, we identified 24 new zebrafish mutants that display impaired intrahepatic biliary network formation. Complementation tests suggested these 24 mutations affect 24 different genes. We applied unsupervised clustering algorithms to unbiasedly classify the recovered mutants into three classes. Further computational analysis revealed that each of the recovered mutations in these three classes has a unique phenotype on node-subtype composition and distribution within the intrahepatic biliary network. In addition, we found most of the recovered mutations are viable. In those mutant fish, which are already good animal models to study chronic cholestatic liver diseases, the biliary network phenotypes persist into adulthood. Altogether, this study provides unique genetic and computational toolsets that advance our understanding of the molecular pathways leading to biliary system malformation and cholestatic liver diseases.

Graphical Abstract

---

[*] Corresponding author. Department of Inflammation and Immunity, Lerner Research Institute of Cleveland Clinic, Cleveland, OH, 44195, USA. sakagut2@ccf.org (T.F. Sakaguchi).

[1] These authors contributed equally to this work.

CRediT authorship contribution statement

Divya Jyoti Singh: Data curation. **Kathryn M. Tuscano:** Data curation, Formal analysis, Project administration, Validation, Writing – review & editing. **Amrhen L. Ortega:** Data curation, Writing – review & editing. **Manali Dimri:** Data curation. **Kevin Tae:** Software, Visualization. **William Lee:** Software. **Muslim A. Muslim:** Data curation. **Isabela M. Rivera Paz:** Data curation. **Jay L. Liu:** Data curation. **Lain X. Pierce:** Data curation, Writing – review & editing. **Allyson McClendon:** Data curation, Formal analysis, Writing – review & editing. **Isabel Gibson:** Data curation. **Jodi Livesay:** Data curation. **Takuya F. Sakaguchi:** Conceptualization, Formal analysis, Funding acquisition, Project administration, Software, Supervision, Validation, Visualization, Writing – original draft, Writing – review & editing.

Appendix A. Supplementary data

Supplementary data to this article can be found online at https://doi.org/10.1016/j.ydbio.2024.05.005.

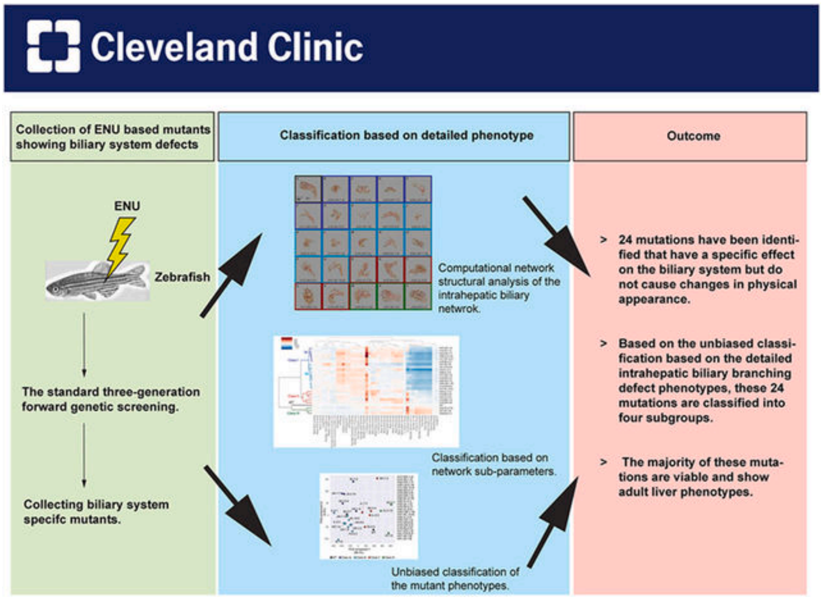

> 24 mutations have been identified that have a specific effect on the biliary system but do not cause changes in physical appearance.

> Based on the unbiased classification based on the detailed intrahepatic biliary branching defect phenotypes, these 24 mutations are classified into four subgroups.

> The majority of these mutations are viable and show adult liver phenotypes.

Keywords

Forward genetics; Intrahepatic biliary network; Branching morphogenesis; Machine learning; Biliary atresia; Cholestatic liver disease

1. Introduction

Cholestatic liver diseases are characterized by slowed or blocked bile flow within the liver and are found in patients of almost any age (Hirschfield et al., 2010; Jansen et al., 2017). Biliary atresia, a cholestatic liver disease affecting neonatal patients, occurs in approximately one in 10,000 live births (Leyva-Vega et al., 2010; Sokol et al., 2003) and is characterized by blockage, underdevelopment, and malformation of the biliary ducts, leading to buildup of bile and, ultimately, scarring and cirrhosis of the liver. Biliary atresia continues to be the most common indication for necessitated liver transplantation and accounts for almost 50% of all liver transplantation performed in children (Sokol et al., 2003). In general, cholestatic liver diseases are caused by a disequilibrium between the loss of biliary epithelial cells (BECs, also called cholangiocytes) and the generation of new BECs. Liver cholestasis could thus be induced by a variety of upstream signaling pathways such as activation of death receptors, immune-mediated injury, or oxidative stress (Hirschfield et al., 2010). Identifying signaling pathways that may induce biliary disease is an important step in understanding these diseases, but much is still unknown. Indeed, relatively few genes which regulate biliary system morphogenesis have been found (Heathcote, 2007; Lemaigre and Zaret, 2004); therefore, forward genetic screens could find more genes responsible for this process. Identifying new genes will lead to the discovery of genes susceptible to cholestatic liver diseases and provide new animal models for such diseases.

Systematic forward genetic screens have led to the identification and characterization of genetic pathways regulating many biological processes, including morphogenesis (Jorgensen and Mango, 2002; Kile and Hilton, 2005; Patton and Zon, 2001; St Johnston, 2002). Historically, classifications of mutant phenotypes collected through genetic screens were decided subjectively where observers decided on classification criteria based on biological knowledge. In contrast, machine learning-based unsupervised classification is an objective process of grouping in which a dataset is sorted based on similarity without any ground truth or pre-labeling of data (Mitchell, 1997). Unsupervised learning approaches are widely used to make partitioning observations into homogenous clusters as well as uncover subpopulation structures of hidden relationships in a given dataset (James et al., 2013; Kiselev et al., 2019). This approach has proven to be a powerful tool for exploring genomics and other omics high-dimensional data sets, yet its usefulness for unbiased mutant phenotype characterizations has not been intensively tested.

The zebrafish transgenic line *Tg(Tp1-MmHbb:EGFP)^{um14}*, which is generated by conjugating tandem *RBP-Jk* response element repeats with enhanced green fluorescent protein (EGFP), expresses EGFP specifically in the intrahepatic biliary network in the zebrafish liver (Lorent et al., 2010; Parsons et al., 2009). This transgenic line allowed us to visualize the entire intrahepatic biliary network in zebrafish larvae, greatly facilitating investigation of the development of the biliary system. Utilizing this transgenic line, we previously developed computational algorithms to convert complex three-dimensional network structures into arrays of numeric sub-parameters to quantify the subtle differences in intrahepatic biliary network branching patterns (Dimri et al., 2017). Precise computational quantification of the intrahepatic biliary network enabled us to unbiasedly quantify mutant phenotypes and break down complicated three-dimensional branching patterns into multi-dimensional arrays, which we can feed into unsupervised classification algorithms.

In this study, we conducted a forward genetic screen for new mutants showing specific phenotypes in the intrahepatic biliary network, and we recovered 24 of these mutants. We applied computational network analysis alongside unsupervised classification algorithms to elucidate phenotype groups and unbiasedly reveal new classes of mutant phenotypes. Together, these studies lay the foundation for integrating unsupervised approaches with genetic screening and provide new biological resources to study biliary system biology.

2. Results

2.1. A forward genetic screen identified 24 mutants affecting intrahepatic biliary network formation

We have previously developed a computational method to precisely quantify network structural properties of the zebrafish intrahepatic biliary network (Dimri et al., 2017). This method allowed us to characterize subtle differences in network branching and connection patterns. Here, we applied this method to facilitate a forward genetic screen. We completed a forward genetic screen to identify mutants showing altered *Tg(Tp1-MmHbb:EGFP)^{um14}* expression in the intrahepatic biliary network at 5 days post-fertilization (dpf) (Materials and Methods). During the screening and recovery procedure, we frequently used the computational skeletal analysis algorithm (Dimri et al., 2017) to confirm the subtle branching differences we observed in the intrahepatic biliary network of mutant larvae were significantly different from those in wild-type larvae. Because we wanted to identify mutations specifically affecting biliary system morphology, we have excluded any mutations that induced general body shape change, obvious pigmentation change, altered morphology of observable organs, defects in blood circulation, or cardiac edema. Although we observed some interesting biliary system phenotypes in mutants with such observable morphological changes during the screening, we excluded them because the mutations causing such phenotypes had already been intensively screened (Driever et al., 1996; Haffter et al., 1996). In the F3 generation, we identified 28 mutations that fit our screening criteria and eventually recovered 24 mutations in the next generation (Table 1). These 24 mutants show consistent phenotypes even after nine or more backcrosses to the original wild-type strain. After we outcrossed the recovered mutants to the wild-type strain for at least five generations, we initiated precise characterization of mutant phenotypes in the intrahepatic biliary network by applying the computational skeletal analysis algorithm (Dimri et al., 2017) (Fig. 1) (Materials and Methods). We converted branching patterns in the *Tg(Tp1-MmHbb:EGFP)*^{um14} expressing intrahepatic biliary network to computational skeletal representation images and corresponding numeric array datasets. We found these 24 mutants show unique branching patterns in the intrahepatic biliary network different from those of the wild-type larvae at 5 dpf (Fig. 1). We did not observe any overt difference in physical appearance among those 24 recovered mutant larvae at 5 dpf, suggesting those mutations specifically affect the biliary system. Thus, we established 24 mutant alleles responsible for unique intrahepatic biliary network branching phenotypes.

2.2. Classification of recovered mutants based on structural sub-parameters of the intrahepatic biliary network

Because the skeletal network analysis produces high-dimensional numeric array data of the intrahepatic biliary network in individually examined larva, we applied the hierarchical clustering heat map algorithm (James et al., 2013) to analyze this data. For each genotype, we first calculated the mean values of each sub-parameter obtained from the initial skeletal conversion. The sample size for each mutant used for analysis is summarized and shown in Table 1. We then used the mean values to apply the clustered heat map algorithm to generate the heat map (Fig. 2) showing the phenotypical similarities between all mutants recovered. This is a completely unbiased classification based solely on the structural sub-parameters of the intrahepatic biliary network. Based on the dendrogram of the clustering heat map data (Fig. 2), we assigned three major mutant phenotype classes: Class I, Class II, and Class III. We found mutants belonging to Class I show decreased total number of segments within the intrahepatic biliary network, indicating this structural sub-parameter is important for the classification of this group. Based on the dendrogram, this class can be further divided into Class Ia and Class Ib, in which mean network density is increased or decreased, respectively. In both Class II and III, the mean network density is increased compared to that in wild-type larvae, but while the total segment number in Class II is relatively consistent, segment number is increased in Class III. Together, these findings suggest that, among all network structural sub-parameters, the total segment number and mean density are relatively more important features among the network structural sub-parameters for classifying recovered mutant phenotypes.

It is possible, however, that the use of clustered heat map analysis does not always respect the intrinsic relationships of mutant phenotypes. In order to independently confirm the phenotypical relationships, we have applied principal component analysis (PCA) (James et al., 2013), which is a different dimensionality-reduction algorithm (Fig. 3). First, we plotted based on the mean network sub-parameter values of each allele (Fig. 3A), and we found that the mutant phenotype classes assigned based on the clustered heat map analysis were grouped together in the plot, suggesting that both algorithms classified the phenotypes similarly. Since PCA-based analysis is important, we next plotted all individual wild-type and mutant larvae analyzed in this study (Table 1) and labeled them based on the assigned classes (Fig. 3B). Each class of mutants had a distribution pattern that partially overlapped but was still distinct from other groups (Fig. 3B), suggesting that this analysis could be used to assign new mutants to these classes.

2.3. Combination of different node sub-types constructs the intrahepatic biliary network

We previously reported that in wild-type larvae at 5 dpf, the distribution ratios of 3-way, 4-way, and 5-way nodes in the intrahepatic biliary network are relatively constant (Dimri et al., 2017). Here, we further analyzed node types in wild-type larvae at 5 dpf by subdividing into node sub-types: 3-way, 4-way, and 5-way nodes can be subdivided into 3, 4, and 5 node subtypes, respectively (Fig. 4A and B) (Table 2). For instance, there are 3 sub-types of 3-way nodes: a 3-way node connecting to three other nodes (3W3N0E), a 3-way node connecting to two other nodes and one endpoint (3W2N1E), and a 3-way node connecting to one other node and two endpoints (3W1N2E). In wild-type larvae at 5 dpf, these node subtypes show a typical distribution ratio in which the 3W2N1E node ratio (35.74% ± 8.18 s.d.) is always higher than that of the 3W1N2E node (0.93% ± 3.02 s.d.) (Fig. 4C). Similarly, among the 4-way nodes, the ratio of the 4W3N1E (7.60% ± 2.30 s.d.) node is always higher than that of the 4W1N3E (0.97% ± 0.92 s.d.) node (Fig. 4D). A similar pattern is observed in 5-way node subtypes (Fig. 4E). In wild-type larvae, the zebrafish intrahepatic biliary network branching patterns are not identical from one larva to another; however, these data together indicate there are certain rules and ranges governing the composition of node-subtypes constructing the intrahepatic biliary network in wild-type larvae.

Next, we investigated node sub-type distributions in all recovered mutants to find which mutation has the strongest effect on these distributions (Supplementary Fig. 1). Although each of the many mutations has a unique effect on the node sub-type distribution, we found that among the 24 mutants, the *lri31* mutation has the strongest effect on 3-way node sub-type distribution. In *lri31* mutant larvae, the ratio of the 3W2N1E (14.26% ± 13.68 s.d.) node is no longer significantly different from that of the 3W1N2E node (33.16% ± 14.84 s.d.) (Fig. 4F), suggesting the *lri31* gene influences the 3-way node sub-type distribution. Similarly, among the recovered mutants, 4-way node subtype distribution is most affected in *lri26* mutant larvae, in which the ratio of 4W4N0E (3.16% ± 1.77 s.d.) is no longer significantly higher than that of 4W1N3E (2.55% ± 1.41 s.d.) (Fig. 4G). 5-way node subtype distribution is most affected in *lri17* mutant larvae, in which the ratio of 5W4N1E (1.03% ± 1.17 s.d.) is no longer significantly higher than that of 5W1N4E (1.40% ± 1.15 s.d.) (Fig. 4H). These mutants that strongly affect node subtype distribution belong to class ib, suggesting that genes belonging to this class may play important roles in regulating node subtype distribution. Together, these data suggest we have identified mutations that influence the proper distribution of node subtypes constructing the intrahepatic biliary network.

2.4. Network structural heat map based characterization of class III mutant phenotypes

The connection property distribution analysis revealed that in mutant larvae belonging to Class III, lri20, lri27, and lri38, node-node connections become thicker than those in wild-type (Fig. 2). In the liver, however, where these thicker node-node connections are localized is not clear. To test the hypothesis that property altered connections could be distributed in a particular area of the liver in these mutants, we have developed additional visualization programs. We previously generated an algorithm to make two-color network heat maps indicating network crowdedness (Dimri et al., 2017). We modified the procedure (Materials and Methods) to generate a seven-color network heat map of the intrahepatic biliary network in wild-type larvae showing the density of the network (Fig. 5A). Because recovered mutants belonging to Class III show a phenotype that increases network density, we first generated seven-colored network density heat maps for *lri20*, *lri27* and *lri38* mutant larvae at 5 dpf (Fig. 5B–D). Consistent with the initial analyses, these mutants show increased network density; however, the network density appears to become much higher in a particular area in the liver when compared to the remainder of the liver (Fig. 5B–D), suggesting the network density increases locally inside the liver.

We then hypothesized network density might increase where segments are thicker in mutants belonging to Class III. However, when we generated network heat maps indicating connection thickness in *lri20*, *lri27* and *lri38* mutant larvae (Fig. 5F–G), we found the network thickness was increased uniformly across the entire network in these mutants compared to that of wild-type larvae (Fig. 5E). Thus, we concluded that connection thickness and density are determined independently in these mutants. We also generated network heat maps indicating connection segment length in *lri20*, *lri27* and *lri38* mutant larvae (Fig. 5J-L), and we found the distribution of longer connections only appeared to be different from those in wild-type larvae in *lri27* mutant larvae (Fig. 5I). Together, these data highlight the usefulness of generating network heat maps to understand where significant property changes develop in the liver.

2.5. Mutations that affect the integrity of the intrahepatic biliary network

Among 24 recovered mutants, we found 4 mutants belonging to Class I show the additional phenotype in which some *Tg(Tp1-MmHbb:EGF-P)*^{um14}-expressing biliary epithelial cells (BECs) segregate from the intrahepatic biliary network. Here, we referred to this phenotype as the BEC segregation phenotype (Table 1). For instance, in *lri31* mutant larvae at 5 dpf, single *Tg(Tp1-MmHbb:EGFP)*^{um14}-expressing BECs located in the anterior part of the liver segregate from the continuous intrahepatic biliary network (Fig. 6B). Meanwhile, all *Tg(Tp1-MmHbb:EGFP)*^{um14}-expressing BECs are always connected to the one continuous intrahepatic biliary network in wild-type larvae (Fig. 6A). The segregated single BECs frequently make direct contact with the *Tg(kdrl:RFP_CAAX)*^{y171}–expressing intrahepatic vascular network (Fig. 6B and C). These data indicate these four genes are responsible for maintaining the integrity of the continuous network.

2.6. Some recovered mutants show biliary system phenotypes in the adult liver

Likely because we screened for mutants showing no gross morphological phenotype, the majority of mutations we collected in this screen are viable (19 out of 24) (Table 1). We hypothesized these viable mutations might continue to affect the intrahepatic biliary network in the adult stage. To test this hypothesis, we collected recovered mutant larvae at 5 dpf and raised homozygous mutant fish into the adult stage. We then examined *Tg(Tp1-MmHbb:EGFP)*^{um14} expression in the adult liver (6 months post-fertilization) of these homozygous mutant fish (Fig. 7). In the wild-type adult liver, *Tg(Tp1-MmHbb:EGFP)*^{um14} remains expressed in the intrahepatic biliary network (Fig. 5A). In the liver of *lri37* mutant fish, *Tg(Tp1-MmHbb:EGFP)*^{um14} expression in the liver appears similar to that of the wild-type (Fig. 7B), suggesting the intrahepatic biliary network is impaired in *lri37* mutant larvae but recovers in adult fish. *Tg(Tp1-MmHbb:EGFP)*^{um14} expression in the liver of *lri26* (Fig. 7C) and *lri14* (Fig. 7D) mutant adult livers, however, is slightly reduced compared to that of wild-type fish, suggesting the intrahepatic biliary network in these mutant fish is reduced. The intrahepatic biliary network is almost lost in the *lri13* (Fig. 7E), *lri21* (Fig. 7F), and *lri24* (Fig. 7G) mutant adults, suggested by *Tg(Tp1-MmHbb:EGFP)*^{um14} expression in the liver being greatly reduced and nearly missing. Finally, in *lri29* (Fig. 7I) and *lri20* (Fig. 7J) mutant adult livers, the *Tg(Tp1-MmHbb:EGFP)*^{um14}-expressing intrahepatic biliary network becomes thicker compared to that of the wild-type adult liver, suggesting the failure of BEC segregation might cause thicker networks to form in these mutant fish. Together, these data indicate we have established new zebrafish models for adult biliary system defects, which can potentially be used as cholestatic liver disease animal models.

2.7. Discussion

In this study from a forward genetic screen, we have recovered 24 new mutants which show specific defects in the branching patterns of the intrahepatic biliary network. This screen was successful only because we utilized the previously developed network structure analysis algorithm to confirm the subtle difference in the branching patterns. Using the algorithm, we converted the phenotypic difference in these 24 mutants into multi-dimensional arrays and applied machine-learning-based unsupervised classification approaches. These approaches objectively classified these 24 mutants into three major classes and quantified phenotypical similarities among them.

The clustered heat map displays a large amount of data in an intuitive format to facilitate the detection of hidden structures and relations in the dataset. We classified recovered mutant phenotypes based on this algorithm. The key question to be evaluated is the extent to which unsupervised clustering reflects the signaling pathways regulated by the mutated genes. Until recently, mapping of a causative mutation of ENU mutagenesis-derived mutants was an extremely labor-intensive process. The development of next-generation sequencing-based approaches (Hill et al., 2013; Leshchiner et al., 2012; Miller et al., 2013; Schneeberger, 2014) has, however, made this process significantly easier. In fact, we have already identified that the *lri35* mutation disrupts the *nckap1l* gene solely by using a decent size (total 22 million reads) RNAseq dataset (Ghaffari et al., 2021). We initially focused on the *nckap1l*^{lri35} mutation because its phenotype is the most similar to that of Cdk-5 suppressed larvae based on the Euclidean distance of the network sub-parameters (Ghaffari et al., 2021). We then demonstrated the *lri35* mutation genetically interacts with the Cdk5 pathway (Ghaffari et al., 2021), thus highlighting precise phenotype quantification can predict the signaling pathway the mutation disrupts. Indeed, utilizing hierarchical clustering methods, the phenotype of the $nckap1l^{lri35}$ mutant most closely resembles that of the *lri12* mutant. This assessment was derived exclusively from the precise quantification and categorization of each mutant phenotype before knowing the mutated genes. Furthermore, we demonstrate that the *lri12* mutation perturbs *dixdc1b* function, and interestingly, *dixdc1b* operates as a downstream effector of *nckap1l* (K. M.T., I.M.R., and T.F.S, under review). These findings collectively prove that our assay has the potential to predict the signaling pathways impacted by specific mutations prior to their explicit identification.

Previously, we have shown that the Cdk5/Pak1/LimK/Cofilin pathway regulates the intrahepatic bile duct network formation (Dimri et al., 2017). In this forward genetic screen, we also identified two class Ib mutants (lri12 and lri35) that also function in the Cdk5 pathway. A large-scale GWAS analysis of Biliary Atresia (BA) patients identified the SNP on the human PAK1 gene as associated with BA (Glessner et al., 2023), suggesting that the Cdk5 pathway is also involved in the pathogenesis of BA. Thus, further identification of the mutated genes of the mutants collected in this study, especially genes belonging to class Ib, would further reveal molecular pathways regulated by Cdk5 that may contribute to the pathogenesis of BA.

Genetic complementation tests within the same subclass have been completed and none of the tested pairs within the same class complemented one another, suggesting these 24 mutations affect 24 different genes. However, different alleles on the same gene could potentially produce very distinct phenotypes which could be classified into different subclasses, thus, it is still possible some recovered mutations affect the same gene. It should be noted that, during the complementation test, there were a few cases in which less than five percent of offspring showed much milder phenotypes than those seen in their parents. Since all recovered mutations are full penetrant and recessive, we concluded these results could be due to genetic interaction between two loci. We observed such genetic interactions between *lri12 (AK-8.5)* and *lri35 (JW-1.10)*, and between *lri37 (KL-10.6)* and *lri29 (IL-2.3)*. We have found that *lri12* and *lri35* mutate different genes. However, further analysis is needed to identify the genes mutated by *lri37 (KL-10.6)* and *lri29 (IL-2.3)*. The number of mutants we recovered from this screening is significantly higher than the number of genes already known to be involved in zebrafish biliary system formation (Brandt et al., 2020; Delous et al., 2012; EauClaire et al., 2012; Ellis et al., 2022; Gao et al., 2019; Sadler et al., 2005; Schaub et al., 2012; Thestrup et al., 2019; Wu et al., 2023). Identifying the responsible genes mutated by these mutations, therefore, will reveal previously unappreciated genes playing essential roles in biliary system formation. The complementation test results also indicated a genetic screen focusing on the biliary system has not been saturated and thus more mutations remain to be discovered.

The Notch signaling pathway plays a pivotal role in the formation of the intrahepatic biliary system (Lorent et al., 2004; Zhao et al., 2022). Concurrently, the Notch pathway is implicated in cardiac development, often correlating with cardiac edema. Given our rigorous screening criteria, mutants manifesting cardiac edema were omitted. Consequently, mutations in the Notch pathway may have been potentially excluded from this screening.

In this study, we redefined node subtypes existing in the wild-type intrahepatic biliary network (Fig. 4). This analysis provided a previously undescribed view on how the network is constructed. We found two node subtypes, 3W3N0E and 3W2N1E, compose more than 65% of the total nodes in the wild-type intrahepatic biliary network at 5 dpf (Fig. 4A). Other node subtype distributions are relatively constant among wild-type larvae at 5 dpf (Fig. 4A), and we found several mutants, including *lri31*, that influence the patterned distributions of node subtypes (Fig. 4, Supplementary Fig. 1). Identifying the responsible genes affected by these mutations will further address molecular pathways responsible for node subtype determination and distribution.

We showed mutant larvae belonging to Class III display increased network density of the intrahepatic biliary network at 5 dpf (Fig. 5). We previously reported that pharmacological suppression of Pak1 or Lim kinase also induced a phenotype (Dimri et al., 2017) similar to those mutant larvae belonging to Class III; thus, it could be possible some of the mutants belonging to this class might affect the Pak1 or Lim kinase-mediated signaling pathways.

We also found several mutants in this study in which single biliary epithelial cells segregate from the network (Fig. 7). We only used the remaining continuous biliary network for the skeletal structural analysis as the segregated single cells are not continuous with the network.

Our high-stringency screening criteria led us to collect viable mutations potentiating the generation of double- and triple-mutant fish. It will be intriguing to examine the biliary network phenotypes in double- and triple-mutant larvae of the same class to examine potential genetic interactions. These viable mutants showing adult liver phenotypes are also an important resource for understanding cholestatic liver disease. A community-based study suggested cholestasis may affect as much as 10–20% of the population (Boyer, 2013), though cholestasis remains benign in the majority of cases (Pollock and Minuk, 2017). To our surprise, some adult mutant fish lost almost all *Tg(Tp1-MmHbb:EGFP)*^{um14}-expressing biliary epithelial cells in the liver (Fig. 7) but remain viable and fertile. These data do not exclude the possibility that in these severe phenotypes, transgenic expression may be lost while the actual biliary epithelial cells persist. In human cholestatic liver disease patients, the obstruction of the intrahepatic biliary network frequently leads to hepatic inflammation; thus, it will be important to examine the degree of hepatic inflammation in these mutant fish. These new viable mutations are an important biological resource for modelling different aspects of human cholestatic liver diseases.

We also found biliary network phenotypes in larvae do not always correlate with biliary network phenotypes in the adult liver. For instance, *lri14* mutant larvae show a reduced complexity phenotype in the biliary network (Class Ia), whereas *lri13* mutant larvae show a crowded biliary network phenotype (Class III). These two mutant fish, however, show very similar biliary network phenotypes in the adult liver (Fig. 7; Table 1). These data suggest that in many cases, the mutations affecting larval biliary network formation also influence the intrahepatic biliary network in adults, but the detailed biliary phenotypes in adults still need to be examined independently from those of larvae.

Overall, this study combined a zebrafish forward genetic screen with unsupervised classifications to identify 24 new mutations which affect different aspects of biliary network formation and maintenance. These mutations will be a tremendous resource to further understand the molecular pathways governing biliary system formation and molecular pathologies leading to cholestatic liver diseases.

3. Materials and Methods

3.1. Zebrafish husbandry and transgenic lines

Zebrafish (*Danio rerio*) larvae were obtained from natural crosses of the wild-type AB/TL strain or heterozygous mutant fish. The following transgenic lines were used: *Tg(Tp1-MmHbb:EGFP)*^{um14} (Parsons et al., 2009) and *Tg(kdrl:RFP_CAAX)*^{y171}(Fujita et al., 2011). We also used 24 new recovered mutants (Table 1), which were generated in this study. Animal husbandry methods were approved by the Cleveland Clinic's Institutional Animal Care and Use Committee.

3.2. Mutant recovery from ENU-based mutagenesis

The standard three-generation screen was conducted in our lab as previously described (Driever et al., 1996; Haffter et al., 1996). In brief, a total of 228 F2 families representing 332.32 genomes were screened for altered *Tg(Tp1-MmHbb:EGFP)*^{um14} expression in the liver at 5 dpf, and 24 mutants were recovered and established. The recovered mutants were backcrossed to the original AB/TL strain for five or more generations before starting detailed phenotype analyses.

3.3. Imaging and computational network structure analysis

Confocal z-stack data of *Tg(Tp1-MmHbb:EGFP)*^{um14} expression in the liver were obtained using a Leica SP5 confocal microscope as previously described (Schaub et al., 2012). The z-step used on the images was 0.42 μm. We used Imaris 8.2 software (Bitplane) to digitally crop the image so only EGFP expression from the intrahepatic biliary network remained for further analysis. The Surface feature was used to isolate the biliary network, and the background subtraction threshold adjusted until the network was continuous. The Liver Analysis Program 5.3 (Dimri et al., 2017) was used for all computational network structure analyses. For all analyses, we confirmed the proper skeletal conversion by overlaying the original confocal image with the converted skeletal image as previously described (Dimri et al., 2017).

3.4. Clustered heat map-based classification and PCA analysis

Structural sub-parameters of the intrahepatic biliary network in recovered mutant larvae were calculated by the Liver Analysis Program 5.3 as described above. Each sub-parameter value was normalized to the mean value in wild-type larvae. The clustering hierarchical heat-map (James et al., 2013) was generated based on the normalized mean values of recovered mutant larvae. Both mean and individual values of structural sub-parameters of each mutant larva were used to generate a PCA plots (James et al., 2013; Kang et al., 2021). The number of samples used per mutant was described in Table 1.

3.5. Heat map analysis on connection segment properties

The data output of the Liver Analysis Program 5.3 was used for further data analysis of the biliary network with the Liver Density Analysis Program v1.4 and Liver Segmentation Selection Program v1.0. The Liver Density Analysis Program v1.4 (Dimri et al., 2017) was used for all computational network density analysis. The Liver Segmentation Selection Program v1.0 was used to isolate segmentation groups for creating heat maps. To create a heat map, the data output of the Liver Analysis Program 5.3 was segmented based on the connection properties. The program output a new TIF stack containing only the segments and nodes of interest. This process was repeated for each class interval. The TIF stacks were then added to Imaris as new channels and colored to denote the class interval. Through this method, heat maps were created for branch length, branch thickness, and network density of the biliary network.

3.6. Refined node-type composition calculation

Based on the initial output of the Liver Analysis Program 5.3, we calculated the frequency of node and endpoint appearance per each existing node to determine node sub-types. This calculation script is named as the Node Sub-type Calculation Program v1.1.

3.7. Kernel density estimation based bivariate distribution plots

We averaged the distribution of the length and thickness in each mutant and plotted the kernel density estimation (Silverman, 1998) based on bivariate distribution. The averaging was based on the estimation that the distribution in each mutant was relatively similar.

3.8. Adult liver tissue processing and imaging

Adult fish were dissected to examine altered *Tg(Tp1-MmHbb:EGF-P)*^{um14} expression in the intrahepatic biliary network in the adult liver at 6 months post-fertilization. Once euthanized, the fish were dissected in 1x-D-PBS, the liver and intestines removed, and the liver separated into lobes. The lobe was fixed with 2% Formaldehyde in PEM, washed twice with PBS, and then embedded in 2% GeneMate LowMelt Agarose (Cat. No. E-3126-25) in PBS. The agarose block was sliced at a thickness of 250 µm with Leica VT1000S vibratome. The slices were then stained overnight with Invitrogen DAPI (Cat. No. D1306). *Tg(Tp1-MmHbb:EGFP)*^{um14} expression in the liver was scanned in a z-stack image on a Leica SP5 confocal microscope, and the image was exported from Bitplane Imaris software.

3.9. Statistics

To compare three or more means, one-way ANOVA followed by Tukey's HSD test was used.

Supplementary Material

Refer to Web version on PubMed Central for supplementary material.

Acknowledgements

We thank Madeline Schaub, James Cantrell, Cassandra Bilogan, Kasey Kisewetter, Gregory Naegele and Kimia Ghaffari for helping our forward genetic screen. We thank Saswat Sahoo for the critical reading of the manuscript. We also thank Maria Roufaeil and Katherine Bell for helping computational analyses.

Funding sources

This work was supported by grants from the NIH (R01 DK103637), Cleveland DDRCC (P30 DK084576), Cleveland Clinic LRI Chair's Innovation Research Fund, and Cleveland Clinic Liver Tumor Research Center of Excellence Fund to T.F.S.

Data availability

Data will be made available on request.

References

Boyer JL, 2013. Bile formation and secretion. Compr. Physiol 3, 1035–1078. [PubMed: 23897680]

Brandt ZJ, Echert AE, Bostrom JR, North PN, Link BA, 2020. Core Hippo pathway components act as a brake on Yap and Taz in the development and maintenance of the biliary network. Development 147.

Delous M, Yin C, Shin D, Ninov N, Debrito Carten J, Pan L, Ma TP, Farber SA, Moens CB, Stainier DY, 2012. Sox9b is a key regulator of pancreaticobiliary ductal system development. PLoS Genet 8, e1002754. [PubMed: 22719264]

Dimri M, Bilogan C, Pierce LX, Naegele G, Vasanji A, Gibson I, McClendon A, Tae K, Sakaguchi TF, 2017. Three-dimensional structural analysis reveals a Cdk5-mediated kinase cascade regulating hepatic biliary network branching in zebrafish. Development 144, 2595–2605. [PubMed: 28720653]

Driever W, Solnica-Krezel L, Schier AF, Neuhauss SC, Malicki J, Stemple DL, Stainier DY, Zwartkruis F, Abdelilah S, Rangini Z, Belak J, Boggs C, 1996. A genetic screen for mutations affecting embryogenesis in zebrafish. Development 123, 37–46. [PubMed: 9007227]

EauClaire SF, Cui S, Ma L, Matous J, Marlow FL, Gupta T, Burgess HA, Abrams EW, Kapp LD, Granato M, Mullins MC, Matthews RP, 2012. Mutations in vacuolar H+ -ATPase subunits lead to biliary developmental defects in zebrafish. Dev. Biol 365, 434–444. [PubMed: 22465374]

Ellis JL, Evason KJ, Zhang C, Fourman MN, Liu J, Ninov N, Delous M, Vanhollebeke B, Fiddes I, Otis JP, Houvras Y, Farber SA, Xu X, Lin X, Stainier DYR, Yin C, 2022. A missense mutation in the proprotein convertase gene furinb causes hepatic cystogenesis during liver development in zebrafish. Hepatol Commun 6, 3083–3097. [PubMed: 36017776]

Fujita M, Cha YR, Pham VN, Sakurai A, Roman BL, Gutkind JS, Weinstein BM, 2011. Assembly and patterning of the vascular network of the vertebrate hindbrain. Development 138, 1705–1715. [PubMed: 21429985]

Gao C, Huang W, Gao Y, Lo LJ, Luo L, Huang H, Chen J, Peng J, 2019. Zebrafish hhex-null mutant develops an intrahepatic intestinal tube due to de-repression of cdx1b and pdx1. J. Mol. Cell Biol 11, 448–462. [PubMed: 30428031]

Ghaffari K, Pierce LX, Roufaeil M, Gibson I, Tae K, Sahoo S, Cantrell JR, Andersson O, Lau J, Sakaguchi TF, 2021. NCK-associated protein 1 like (nckap1l) minor splice variant regulates intrahepatic biliary network morphogenesis. PLoS Genet 17, e1009402. [PubMed: 33739979]

Glessner JT, Ningappa MB, Ngo KA, Zahid M, So J, Higgs BW, Sleiman PMA, Narayanan T, Ranganathan S, March M, Prasadan K, Vaccaro C, Reyes-Mugica M, Velazquez J, Salgado CM, Ebrahimkhani MR, Schmitt L, Rajasundaram D, Paul M, Pellegrino R, Gittes GK, Li D, Wang X, Billings J, Squires R, Ashokkumar C, Sharif K, Kelly D, Dhawan A, Horslen S, Lo CW, Shin D, Subramaniam S, Hakonarson H, Sindhi R, 2023. Biliary atresia is associated with polygenic susceptibility in ciliogenesis and planar polarity effector genes. J. Hepatol 79, 1385–1395. [PubMed: 37572794]

Haffter P, Granato M, Brand M, Mullins MC, Hammerschmidt M, Kane DA, Odenthal J, van Eeden FJ, Jiang YJ, Heisenberg CP, Kelsh RN, Furutani-Seiki M, Vogelsang E, Beuchle D, Schach U, Fabian C, Nusslein-Volhard C, 1996. The identification of genes with unique and essential functions in the development of the zebrafish, Danio rerio. Development 123, 1–36. [PubMed: 9007226]

Heathcote EJ, 2007. Diagnosis and management of cholestatic liver disease. Clin. Gastroenterol. Hepatol 5, 776–782. [PubMed: 17628332]

Hill JT, Demarest BL, Bisgrove BW, Gorsi B, Su YC, Yost HJ, 2013. MMAPPR: mutation mapping analysis pipeline for pooled RNA-seq. Genome Res 23, 687–697. [PubMed: 23299975]

Hirschfield GM, Heathcote EJ, Gershwin ME, 2010. Pathogenesis of cholestatic liver disease and therapeutic approaches. Gastroenterology 139, 1481–1496. [PubMed: 20849855]

James G, Witten D, Hastie T, Tibshirani R, 2013. An Introduction to Statistical Learning : with Applications in R Springer, New York.

Jansen PLM, Ghallab A, Vartak N, Reif R, Schaap FG, Hampe J, Hengstler JG, 2017. The ascending pathophysiology of cholestatic liver disease. Hepatology 65, 722–738. [PubMed: 27981592]

Jorgensen EM, Mango SE, 2002. The art and design of genetic screens: caenorhabditis elegans. Nat. Rev. Genet 3, 356–369. [PubMed: 11988761]

Kang JB, Nathan A, Weinand K, Zhang F, Millard N, Rumker L, Moody DB, Korsunsky I, Raychaudhuri S, 2021. Efficient and precise single-cell reference atlas mapping with Symphony. Nat. Commun 12.

Kile BT, Hilton DJ, 2005. The art and design of genetic screens: mouse. Nat. Rev. Genet 6, 557–567. [PubMed: 15951745]

Kiselev VY, Andrews TS, Hemberg M, 2019. Challenges in unsupervised clustering of single-cell RNA-seq data (vol 20, pg 273, 2019). Nat. Rev. Genet 20, 310, 310. [PubMed: 30617341]

Lemaigre F, Zaret KS, 2004. Liver development update: new embryo models, cell lineage control, and morphogenesis. Curr. Opin. Genet. Dev 14, 582–590. [PubMed: 15380251]

Leshchiner I, Alexa K, Kelsey P, Adzhubei I, Austin-Tse CA, Cooney JD, Anderson H, King MJ, Stottmann RW, Garnaas MK, Ha S, Drummond IA, Paw BH, North TE, Beier DR, Goessling W, Sunyaev SR, 2012. Mutation mapping and identification by whole-genome sequencing. Genome Res 22, 1541–1548. [PubMed: 22555591]

Leyva-Vega M, Gerfen J, Thiel BD, Jurkiewicz D, Rand EB, Pawlowska J, Kaminska D, Russo P, Gai X, Krantz ID, Kamath BM, Hakonarson H, Haber BA, Spinner NB, 2010. Genomic alterations in biliary atresia suggest region of potential disease susceptibility in 2q37.3. Am. J. Med. Genet 152A, 886–895. [PubMed: 20358598]

Lorent K, Moore JC, Siekmann AF, Lawson N, Pack M, 2010. Reiterative use of the Notch signal during zebrafish intrahepatic biliary development. Dev. Dynam 239, 855–864.

Lorent K, Yeo SY, Oda T, Chandrasekharappa S, Chitnis A, Matthews RP, Pack M, 2004. Inhibition of Jagged-mediated Notch signaling disrupts zebrafish biliary development and generates multi-organ defects compatible with an Alagille syndrome phenocopy. Development 131, 5753–5766. [PubMed: 15509774]

Miller AC, Obholzer ND, Shah AN, Megason SG, Moens CB, 2013. RNA-seq-based mapping and candidate identification of mutations from forward genetic screens. Genome Res 23, 679–686. [PubMed: 23299976]

Mitchell T, 1997. Machine Learning. McGraw-Hill.

Parsons MJ, Pisharath H, Yusuff S, Moore JC, Siekmann AF, Lawson N, Leach SD, 2009. Notch-responsive cells initiate the secondary transition in larval zebrafish pancreas. Mech. Dev 126, 898–912. [PubMed: 19595765]

Patton EE, Zon LI, 2001. The art and design of genetic screens: zebrafish. Nat. Rev. Genet 2, 956–966. [PubMed: 11733748]

Pollock G, Minuk GY, 2017. Diagnostic considerations for cholestatic liver disease. J. Gastroenterol. Hepatol 32, 1303–1309. [PubMed: 28106928]

Sadler KC, Amsterdam A, Soroka C, Boyer J, Hopkins N, 2005. A genetic screen in zebrafish identifies the mutants, and as models of liver disease. Development 132, 3561–3572. [PubMed: 16000385]

Schaub M, Nussbaum J, Verkade H, Ober EA, Stainier DY, Sakaguchi TF, 2012. Mutation of zebrafish Snapc4 is associated with loss of the intrahepatic biliary network. Dev. Biol 363, 128–137. [PubMed: 22222761]

Schneeberger K, 2014. Using next-generation sequencing to isolate mutant genes from forward genetic screens. Nat. Rev. Genet 15, 662–676. [PubMed: 25139187]

Silverman BW, 1998. Density Estimation for Statistics and Data Analysis. Chapman & Hall/CRC, Boca Raton.

Sokol RJ, Mack C, Narkewicz MR, Karrer FM, 2003. Pathogenesis and outcome of biliary atresia: current concepts. J. Pediatr. Gastroenterol. Nutr 37, 4–21. [PubMed: 12827000]

St Johnston D, 2002. The art and design of genetic screens: Drosophila melanogaster. Nat. Rev. Genet 3, 176–188. [PubMed: 11972155]

Thestrup MI, Caviglia S, Cayuso J, Heyne RLS, Ahmad R, Hofmeister W, Satriano L, Wilkinson DG, Andersen JB, Ober EA, 2019. A morphogenetic EphB/EphrinB code controls hepatopancreatic duct formation. Nat. Commun 10, 5220. [PubMed: 31745086]

Wu C, Zhang W, Luo Y, Cheng C, Wang X, Jiang Y, Li S, Luo L, Yang Y, 2023. Zebrafish ppp1r21 mutant as a model for the study of primary biliary cholangitis. J Genet Genomics 50 (12), 1004–1013. [PubMed: 37271428]

Zhao C, Matalonga J, Lancman JJ, Liu L, Xiao C, Kumar S, Gates KP, He J, Graves A, Huisken J, Azuma M, Lu Z, Chen C, Ding BS, Dong PDS, 2022. Regenerative failure of intrahepatic biliary cells in Alagille syndrome rescued by elevated Jagged/Notch/Sox9 signaling. Proc. Natl. Acad. Sci. U.S.A 119, e2201097119. [PubMed: 36469766]

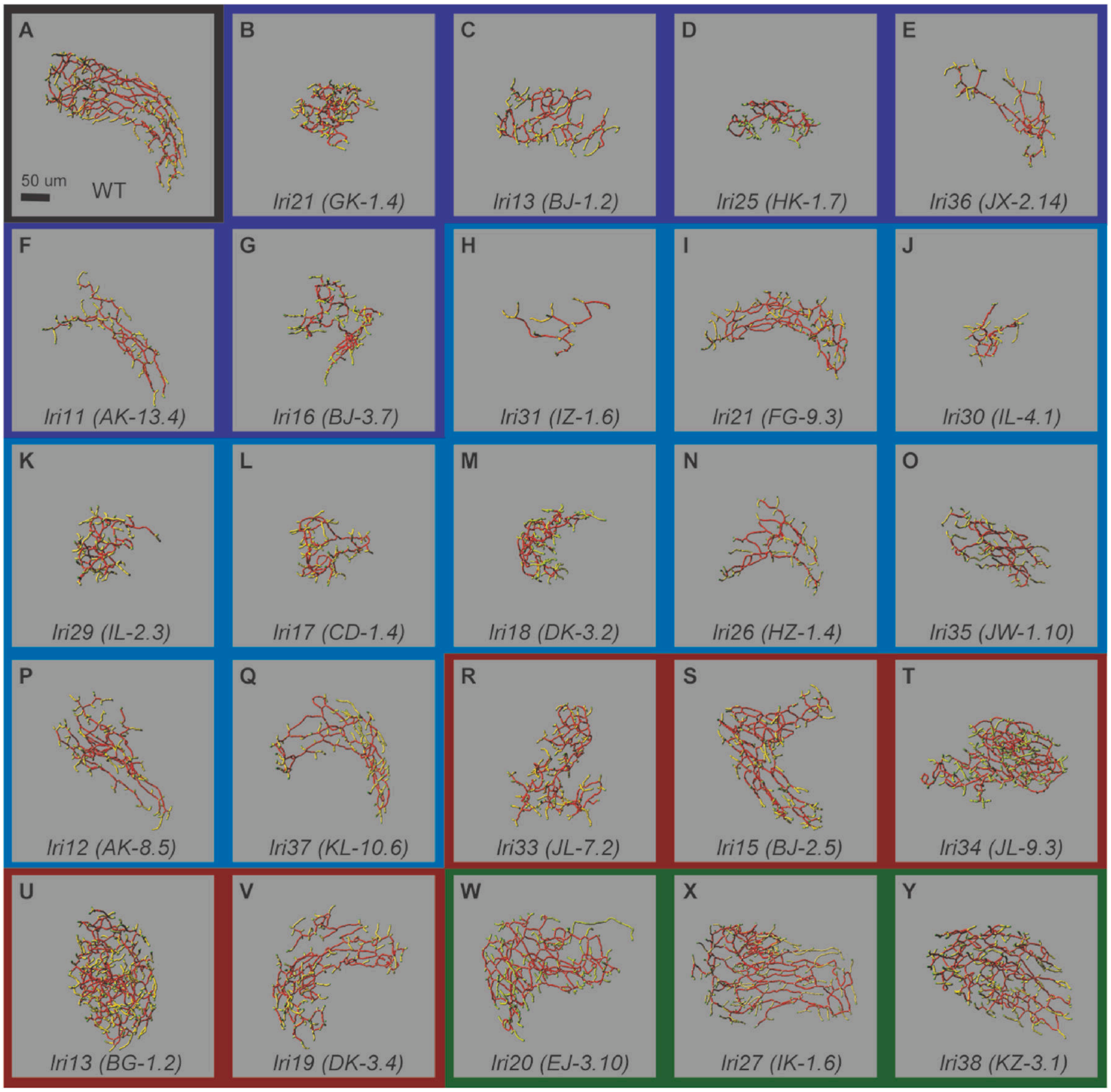

Fig. 1.

Skeletal representation of the intrahepatic biliary network at 5 dpf in mutants recovered from the forward genetic screen. Skeletal representation of the intrahepatic biliary network in mutant larvae based on *Tg(Tp1-MmHbb:EGFP)*^{um14} expression at 5 dpf, unbiasedly classified based on branching sub-parameters of the intrahepatic biliary network. (**A**) Wild-type control (Black border). **(B–G)** Class Ia (Dark Blue border): *Iri24* (*GK-1.4*) (B), *Iri14* (*BJ-1.2*) (C), *Iri25* (*HK-1.7*) (D), *Iri36* (*JX-2.14*) (E), *Iri11* (*AK-13.4*) (F), and *Iri16* (*BJ-3.7*) (G) mutants belong to this class. **(H–Q)** Class Ib (Light Blue border): *Iri31* (*IZ-1.6*) (H), *Iri21* (*FG-9.3*) (I), *Iri30* (*IL-4.1*) (J), *Iri29* (*IL-2.3*) (K), *Iri17* (*CD-1.4*) (L), *Iri18* (*DK-3.2*) (M), *Iri26* (*HZ-1.4*) (N), *Iri35* (*JW-1.10*) (O), *Iri12* (*AK-8.5*) (P), and *Iri37* (*KL-10.6*) (Q) mutants belong to this class. **(R–V)** Class II (Red border): *Iri33* (*JL-7.2*) (R), *Iri15* (*BJ-2.5*) (S), *Iri34* (*JL-9.3*) (T), *Iri13* (*BG-1.2*) (U), and *Iri19* (*DK-3.4*) (V) mutants belong to this class. **(W–Y)** Class III (Green border): *Iri20* (*EJ-3.10*) (W), *Iri27* (*IK-1.6*) (X), and *Iri38* (*KZ-3.1*) (Y) mutants belong to this class. Ventral views, anterior to the top. The network features are color-coded: end points (green), nodes (white), node-node connections (red), and node-end point connections (yellow). The representative biliary skeleton for each genotype was selected based on the lowest deviation from the average network structural sub-parameter attributes.

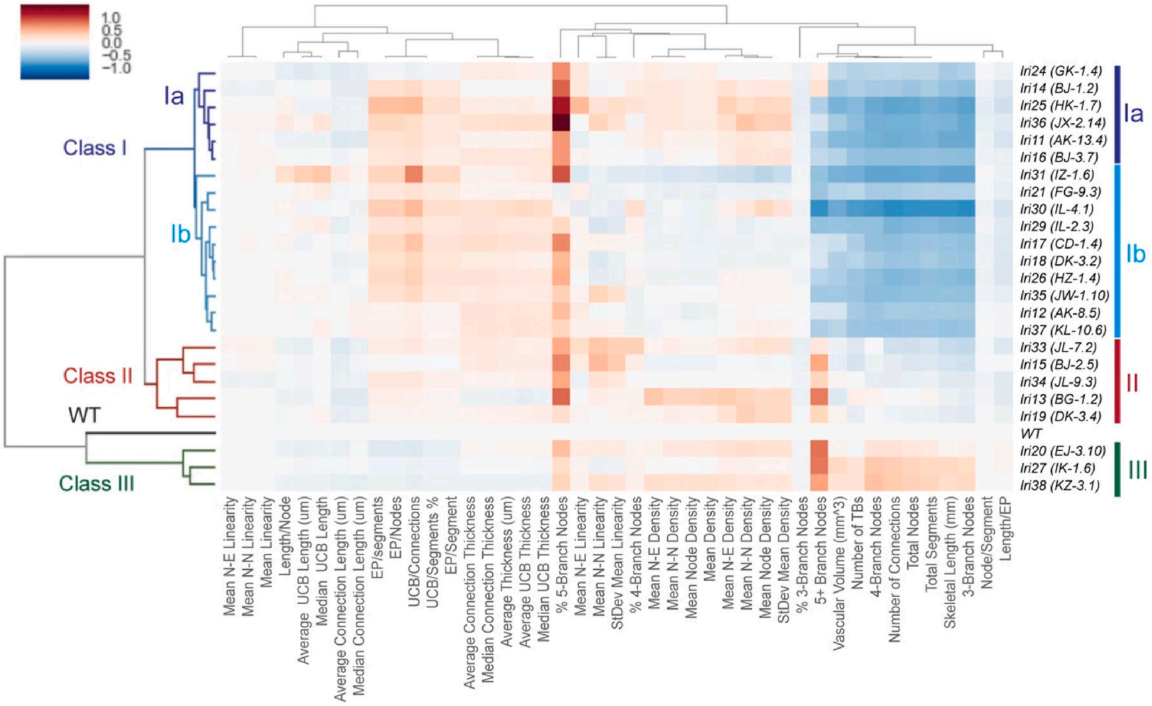

Fig. 2.

Clustered heat map-based classification of recovered mutants. Clustered heat map based on the structural sub-parameters of the intrahepatic biliary network in recovered mutant larvae at 5 dpf. All sub-parameters are normalized to the average value of the corresponding sub-parameters in the wild-type dataset. Clustering was done with the hierarchical clustering algorithm. Red indicates a higher value than wild-type, and blue indicates a lower value than wild-type. Values represent the average for each specimen dataset. The x-axis of the dendrogram indicates the relative similarity of each structural sub-parameter to other sub-parameters. The shorter the line between two sub-parameters, the more closely related they are. Similarly, the y-axis indicates the relative similarity of each mutant phenotype to other mutant phenotypes. Classes are denoted by the color of the y-axis dendrogram: Wild-type (Black), Class Ia (Dark Blue), Class Ib (Light Blue), Class II (Red), and Class III (Green). Classification was unbiasedly based on network structural sub-parameters of the intrahepatic biliary network.

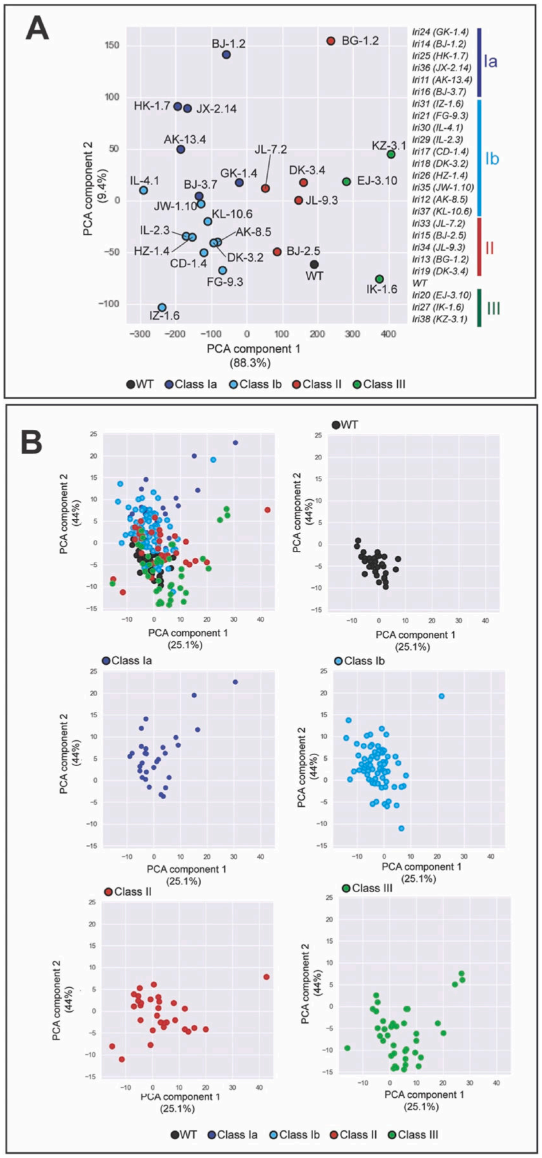

Fig. 3.

Principal component analysis (PCA) dimensionality reduction analysis-based mutant classification. (A) The PCA dimensionality reduction plot of wild-type and recovered mutants based on the mean values of biliary network structural sub-parameters within the allele indicates the similarity of phenotypes. Colors denote the defined class of that specimen group: Wild-type (Black), Class Ia (Dark Blue), Class Ib (Light Blue), Class II (Red), and Class III (Green). Proximity of the data points indicates the relative similarity of the recovered mutants; the closer the points, the more closely related the phenotypes are. **(B)** The PCA plot of all individual larvae of wild-type and recovered mutants analyzed in this study based on biliary network structural sub-parameters. The plot is labeled based on the assigned classes: Wild-type (Black), Class Ia (Dark Blue), Class Ib (Light Blue), Class II (Red), and Class III (Green). The same plots showing only the data from each class are shown separately. Each class of mutants was distributed in a pattern that partially overlapped but was still clearly distinct.

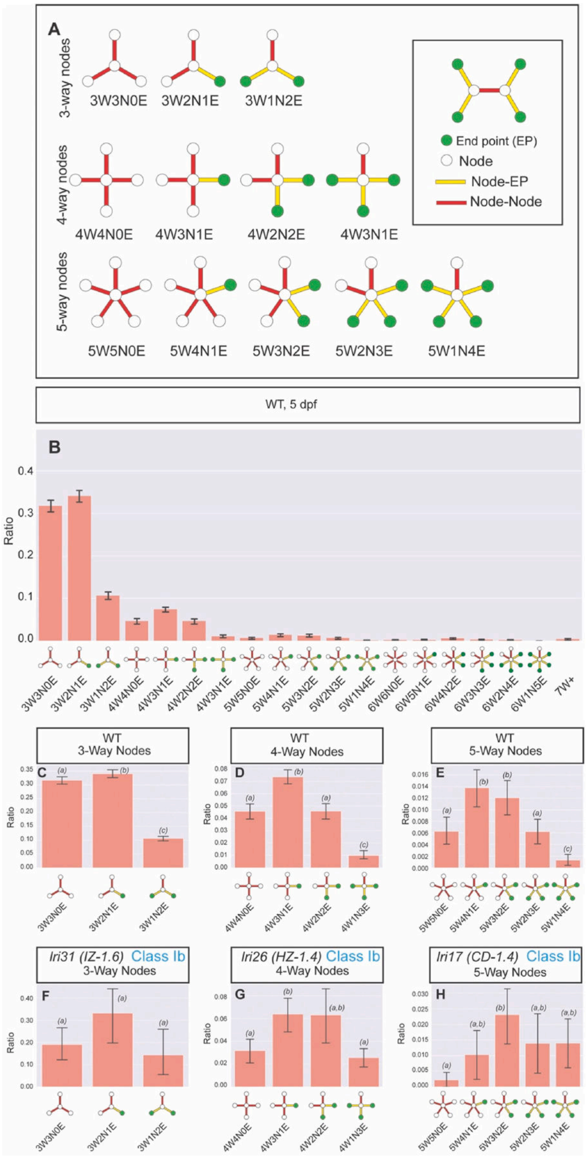

Fig. 4.

Defining the node-type composition of the intrahepatic biliary network. Computational network analysis revealed the intrahepatic biliary network could be defined as a combination of different types of nodes. **(A)** Schematics of node-subtypes existing in the intrahepatic biliary network. **(B)** Ratio of node sub-type distribution in the intrahepatic biliary network in wild-type larvae at 5 dpf. X-axis labels denote the number of branches connected to the node (#W), how many of those branches are node-node connections (#N), and how many of those branches are node-endpoint connections (#E). In the schematics, node (white circle), endpoint (green circle), node-node (red bar) and node-endpoint (yellow bar) connections indicate each node sub-type compositions. **(C)** Ratio of 3-way node sub-types in wild-type (WT) is plotted separately. The 3W2N1E node always exists significantly higher than the 3W1N2E node in WT. **(D)** Ratio of 4-way node sub-types in WT is plotted separately. Similar to the distribution of 3-way nodes, the 4W3N1E node always exists with the highest ratio in WT while the 4W1N3E node is always lower than other node sub-types. **(E)** Ratio of 5-way node sub-types in WT is plotted separately. The 5W1N4E node always exists at the lowest ratio in WT. **(F)** Ratio of 3-way node sub-types in *lri31 (IZ-1.6)* mutant larvae at 5 dpf. The ratio difference between 3W2N1E and 3W1N2E is lost in *lri31* mutant larvae. **(G)** Ratio of 4-way node sub-types in *lri26 (HZ-1.4)* mutant larvae at 5 dpf. The relative ratio of the 4W1N3E node was increased in *lri26* mutant larvae. **(H)** Ratio of 5-way node sub-types in *lri17 (CD-1.4)* mutant larvae at 5 dpf. The relative ratio of the 5W1N4E node is increased in *lri17* mutant larvae. These data indicate the distribution of node sub-types is regulated in part by these mutations. Bars with a shared letter indicate the difference is not statistically significant.

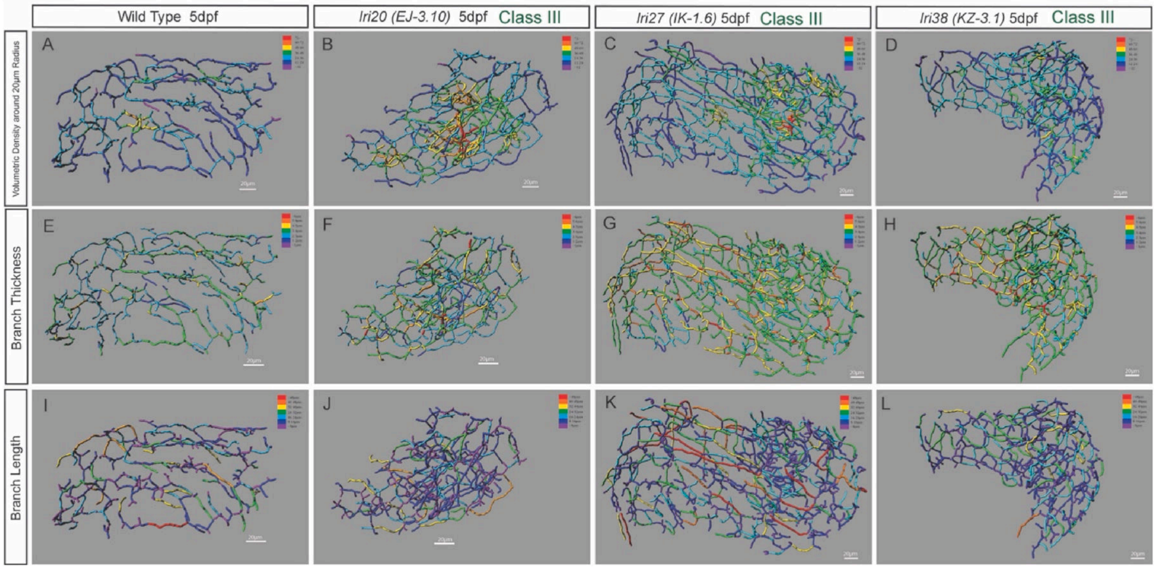

Fig. 5.

Heat map-based characterization of Class III mutant phenotypes. Heat map skeletal representation of the intrahepatic biliary network showing different segment properties in wild-type (WT) and recovered mutant larvae belonging to Class III. The colors of the heat maps indicate value ranges for each segment property. The hotter the color, the higher the value for all heat maps. **(A–D)** Network volumetric density heat map in WT (A), *lri20 (EJ-3.10)* (B), *lri27 (IK-1.6)* (C) and *lri38 (KZ-3.1)* (D) mutant larvae at 5 dpf. Purple represents less than 12 A.U., dark blue represents 12–24 A.U., light blue represents 24–36 A.U., green represents 36–48 A.U., yellow represents 48–60 A.U., orange represents 60–72 A.U., and red represents 72 A.U. and greater. These mutants show increased network density in a particular area in the liver not seen in WT. **(E–H)** Network connection thickness heat map in WT (E), *lri20 (EJ-3.10)* (F), *lri27 (IK-1.6)* (G) and *lri38 (KZ-3.1)* (H) mutant larvae at 5 dpf. Purple represents less than 1 µm, dark blue represents 1–2 µm, light blue represents 2–3 µm, green represents 3–4 µm, yellow represents 4–5 µm, orange represents 5–6 µm, and red represents 6 µm and greater. Network thickness increased uniformly across the entire network in the mutants compared to WT. **(I–L)** Network connection length heat map in WT (I), *lri20 (EJ-3.10)* (J), *lri27 (IK-1.6)* (K) and *lri38 (KZ-3.1)* (L) mutant larvae at 5 dpf. Purple represents less than 8 µm, dark blue represents 8–16 µm, light blue represents 16–24 µm, green represents 24–32 µm, yellow represents 32–40 µm, orange represents 40–48 µm, and red represents 48 µm and greater. Distribution of longer connections was only different from those in WT larvae in *lri27* mutant larvae.

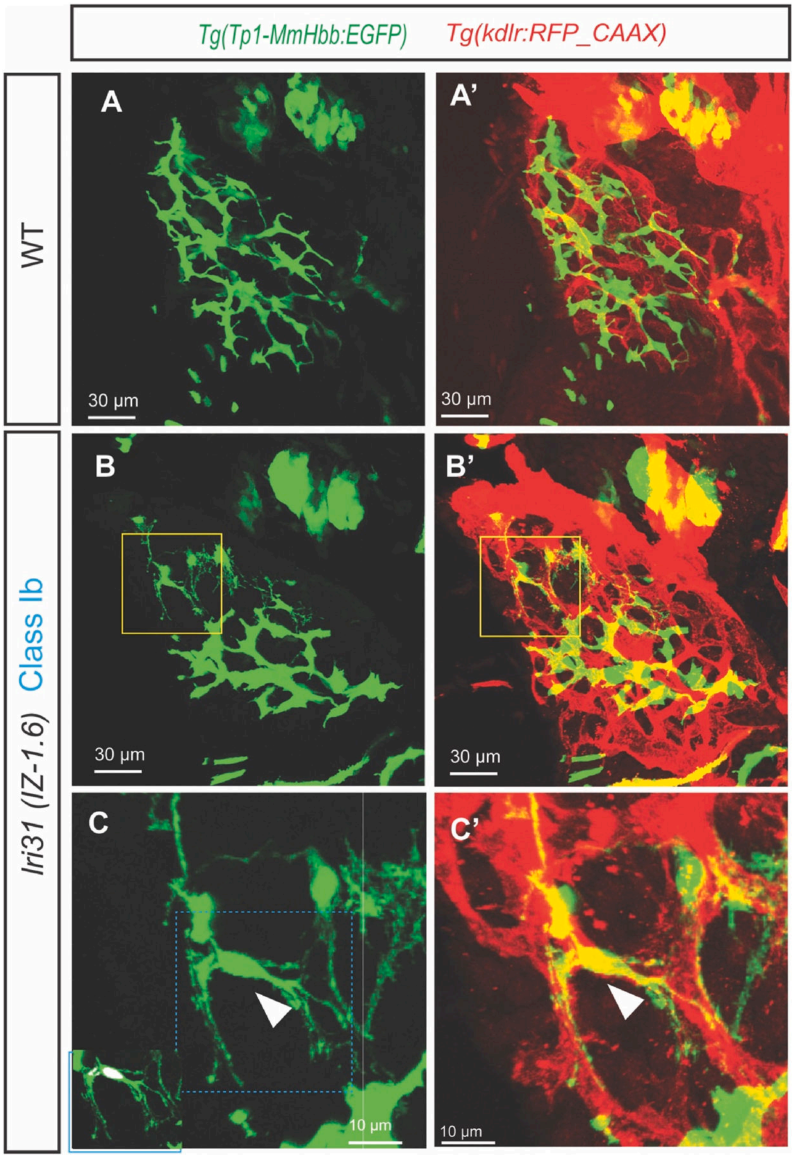

Fig. 6.

Biliary epithelial cells segregate from the intrahepatic biliary network in *lri31 (IZ-1.6)* mutant larvae at 5 dpf. (A–C) Projected confocal images of wild-type (A) and *lri31 (IZ-1.6)* mutant (B and C) larvae visualized for *Tg(Tp1-MmHbb:EGFP)*^{um14} expressions at 5 dpf. *Tg(kdrl:RFP_CAAX)*^{y171} expressions are merged in (A'-C'). Yellow-outlined area in B is magnified and shown in C. Blue-outlined area in C is magnified and merged with the DAPI and GFP co-localization signal in the left bottom corner. Ventral views, anterior to the top. In *lri31 (IZ-1.6)* mutant larvae, single biliary epithelial cells segregate from the intrahepatic biliary network and make physical contact with the intrahepatic vascular network (White arrowhead in C). DAPI and GFP co-localization assays revealed that six BECs are segregated from the main biliary tree in this larva.

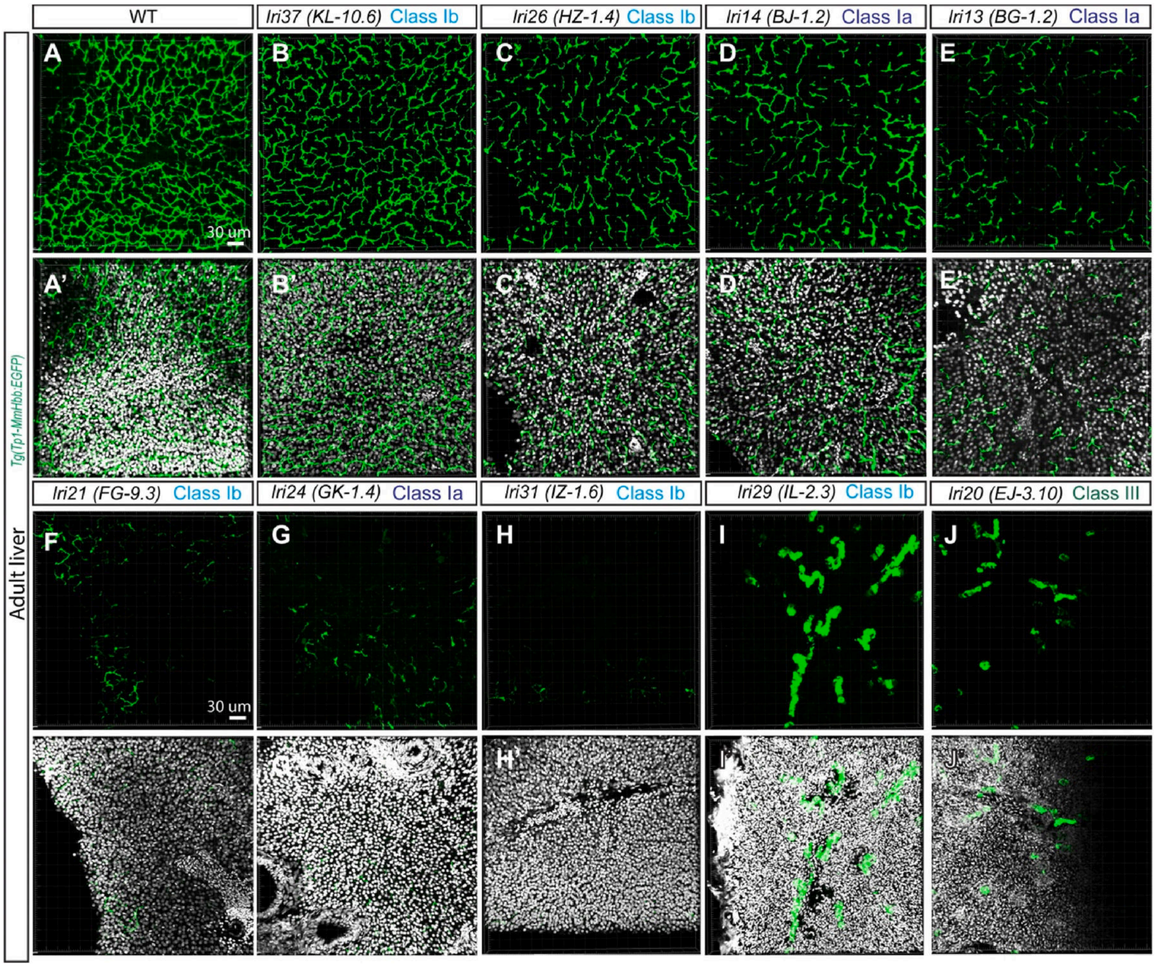

Fig. 7.

Recovered viable mutants show distinguishable phenotypes in the adult liver. (**A-J)** Projected confocal images of the adult liver visualized for *Tg(Tp1-MmHbb: EGFP)*^{um14} expression in wild-type (A), *lri37 (KL-10.6)* (B), *lri26 (HZ-1.4)* (C), *lri14 (BJ-1.2)* (D), *lri13 (BG-1.2)* (E), *lri21 (FG-9.3)* (F), *lri24 (GK-1.4)* (G), *lri31 (IZ-1.6)* (H), *lri29 (IL-2.3)* (I), and *lri20 (EJ-3.10)* (J) mutant fish. DAPI staining is overlaid in (A'-J'). Cross sections of the liver were used. The histology of the liver based on DAPI is significantly altered in lri21 (F'), lri24 (G') and lri21 (J'), possibly due to cholestasis. The z-thickness of all projected images is 0.42 µm.

Table 1

Mutants recovered from the forward genetic screen.

Allele	Screen ID	Mutant Class	Mutation Viability	BEC Segregation	Sample number	Adult Phenotype
lri11	AK-13.4	Class Ia	Viable		6	
lri12	AK-8.5	Class Ib	Viable		8	
lri13	BG-1.2	Class II	Viable		7	Slightly reduced
lri14	BJ-1.2	Class Ia	Viable		9	Slightly reduced
lri15	BJ-2.5	Class II	Viable		9	
lri16	BJ-3.7	Class Ia	Lethal	Yes	8	
lri17	CD-1.4	Class Ib	Lethal	Yes	7	
lri18	DK-3.2	Class Ib	Viable		7	
lri19	DK-3.4	Class II	Viable		5	
lri20	EJ-3.10	Class III	Viable		7	Thickened
lri21	FG-9.3	Class Ib	Viable		5	Greatly reduced
lri24	GK-1.4	Class Ia	Viable		5	Greatly reduced
lri25	HK-1.7	Class Ia	Viable		11	
lri26	HZ-1.4	Class Ib	Viable	Yes	10	Slightly reduced
lri27	IK-1.6	Class III	Viable		15	
lri29	IL-2.3	Class Ib	Viable		9	Thickened
lri30	IL-4.1	Class Ib	Viable		6	
lri31	IZ-1.6	Class Ib	Viable	Yes	5	Greatly reduced
lri33	JL-7.2	Class II	Lethal		5	
lri34	JL-9.3	Class II	Viable		10	
lri35	JW-1.10	Class Ib	Viable		25	
lri36	JX-2.14	Class Ia	Lethal		8	
lri37	KL-10.6	Class Ib	Viable		10	Slightly reduced
lri38	KZ-3.1	Class III	Viable		12	
WT	Wild-Type	WT	Viable		33	

Table 2

Node sub-type distribution in wild-type larvae at 5 dpf.

Node Sub-Type	Average	Standard Deviation
3W3N0E	31.45%	5.18
3W2N1E	35.74%	8.18
3W1N2E	10.93%	3.02
4W4N0E	4.62%	1.92
4W3N1E	7.60%	2.30
4W2N2E	4.81%	2.17
4W1N3E	0.97%	0.92
5W5N0E	0.57%	0.68
5W4N1E	1.49%	1.03
5W3N2E	1.37%	1.07
5W2N3E	0.75%	0.69
5W1N4E	0.16%	0.32
6W6N0E	0.15%	0.27
6W5N1E	0.23%	0.31
6W4N2E	0.51%	0.59
6W3N3E	0.24%	0.37
6W2N4E	0.13%	0.26
6W1N5E	0.00%	0.00